

Retraction

Retracted: Research on the Application of Environmental Art Design Based on the Combination of VR and Panoramic Video Technology

Scientific Programming

Received 8 August 2023; Accepted 8 August 2023; Published 9 August 2023

Copyright © 2023 Scientific Programming. This is an open access article distributed under the Creative Commons Attribution License, which permits unrestricted use, distribution, and reproduction in any medium, provided the original work is properly cited.

This article has been retracted by Hindawi following an investigation undertaken by the publisher [1]. This investigation has uncovered evidence of one or more of the following indicators of systematic manipulation of the publication process:

- (1) Discrepancies in scope
- (2) Discrepancies in the description of the research reported
- (3) Discrepancies between the availability of data and the research described
- (4) Inappropriate citations
- (5) Incoherent, meaningless and/or irrelevant content included in the article
- (6) Peer-review manipulation

The presence of these indicators undermines our confidence in the integrity of the article's content and we cannot, therefore, vouch for its reliability. Please note that this notice is intended solely to alert readers that the content of this article is unreliable. We have not investigated whether authors were aware of or involved in the systematic manipulation of the publication process.

Wiley and Hindawi regrets that the usual quality checks did not identify these issues before publication and have since put additional measures in place to safeguard research integrity.

We wish to credit our own Research Integrity and Research Publishing teams and anonymous and named external researchers and research integrity experts for contributing to this investigation.

The corresponding author, as the representative of all authors, has been given the opportunity to register their

agreement or disagreement to this retraction. We have kept a record of any response received.

References

- [1] Y. Kong, "Research on the Application of Environmental Art Design Based on the Combination of VR and Panoramic Video Technology," *Scientific Programming*, vol. 2021, Article ID 9820550, 11 pages, 2021.

Research Article

Research on the Application of Environmental Art Design Based on the Combination of VR and Panoramic Video Technology

Yingqi Kong 

Wenzhou Business College, Wenzhou 325006, Zhejiang, China

Correspondence should be addressed to Yingqi Kong; 00204434@wzbc.edu.cn

Received 18 September 2021; Revised 21 October 2021; Accepted 22 October 2021; Published 17 November 2021

Academic Editor: Bai Yuan Ding

Copyright © 2021 Yingqi Kong. This is an open access article distributed under the Creative Commons Attribution License, which permits unrestricted use, distribution, and reproduction in any medium, provided the original work is properly cited.

The panoramic video technology is introduced to collect multiangle data of design objects, draw a 3D spatial model with the collected data, solve the first-order differential equation for the 3D spatial model, obtain the spatial positioning extremes of the object scales, and realize the alignment and fusion of panoramic video images according to the positioning extremes above and below the scale space. Then, the panoramic video is generated and displayed by computer processing so that the tourist can watch the scene with virtual information added to the panoramic video by wearing the display device elsewhere. It solves the technical difficulties of the high complexity of the algorithm in the system of panoramic video stitching and the existence of stitching cracks and the “GHOST” phenomenon in the stitched video, as well as the technical difficulties that the 3D registration is easily affected by the time-consuming environment and target tracking detection algorithm. The simulation results show that the panoramic video stitching method performs well in real time and effectively suppresses stitching cracks and the “GHOST” phenomenon, and the augmented reality 3D registration method performs well for the local enhancement of the panoramic video.

1. Introduction

Augmented reality (AR) is an enhancement of the real world. In some real scenes (such as cultural relics and museums) that are not convenient for observers to enter, a panoramic video capture device is placed in the scene to capture the landscape of the real scene, and then the panoramic video is obtained and displayed through computer stitching processing; augmented reality technology is then used to add virtual information to the panoramic video and establish an augmented reality system based on panoramic video imaging [1].

Augmented reality systems are now widely studied at home and abroad and have a wide range of uses. Xue [2] studied scene recognition and tracking registration techniques for mobile augmented reality; Zhao [3] proposed an augmented reality system based on Hanzi markers; Bo et al. [4] proposed a new tracking registration method; Multisilta [5] proposed a tracking registration method based on TLD [6]; and Yu and Wang [7] studied augmented reality system modeling based on visual markers and alignment error

problems. However, there are few studies on augmented reality systems based on panoramic video imaging, and the establishment of a new AR system can help integrate knowledge in various fields and is very innovative.

Panoramic video technology allows videos to be viewed in any direction, free from the constraints of the original viewing angle and providing an authentic sensory experience [8–10]. Today, panoramic video is a popular and widely used form of media that has greatly improved people’s lives. Environmental art design is an important part of digital architectural design, which is the construction and creation of artistic landscapes in a specific context [11]. With the gradual improvement of people’s living standards, the requirements for living and leisure environments have increased. Traditional videos can only provide certain perspectives and cannot present a comprehensive view of the environment, making it difficult for users to grasp the details of the environment, wasting time and costs, and no longer meeting people’s needs [12, 13].

In this paper, we explore and study the application of panoramic video technology in environmental art design by

linking panoramic video technology and environmental art design to the above problems. The application of panoramic video technology provides a solid foundation for a good living environment and creates very convenient living conditions. The panoramic video augmented reality system is proposed, and the key panoramic video stitching technology and augmented reality 3D registration technology to realize the system are proposed based on improved fast ORB (oriented FAST (features from accelerated segment test)) [14] and rotated BRIEF (binary robust independent elementary features). Binary robust independent elementary features [15], feature detection algorithm [16], and improved fast KCF (improved kernelized correlation filters, I-KCF) [17] augmented the reality 3D registration method for target tracking.

1.1. System Principle and Key Technology. The panoramic video augmented reality system can be regarded as composed of two parts: the real scene is a panoramic video camera placed on the circumference of a circle with center O and radius R , and then video images are collected, and the collected videos are stitched together according to the sequential relationship and displayed as the panoramic video background; in the virtual world part, the computer-generated virtual information is placed somewhere between the head display device and the background. If the virtual object is viewed through the head display device, the real background part behind the virtual object will be blocked by the virtual object, and the virtual object is superimposed with the real background through 3D registration technology, so as to realize the purpose of combining reality and imagination [18, 19]. The principle of the AR system with circular panoramic video imaging is shown in Figure 1.

The key technology of the panoramic video augmented reality system is mainly the panoramic video generation technology and 3D registration technology [20]. The specific steps of the system are shown in Figure 2.

1.2. Improved ORB Panoramic Video Generation. The key technology of panoramic video generation is image stitching, and image matching is the core technology of image stitching. The ORB algorithm introduces FAST [1] feature direction to make it rotation invariant because FAST feature points do not have to scale invariant information, so the ORB algorithm does not have to scale invariance [21]. The multiscale space theory is used to extract the stable feature points, and the number and spacing of feature points are parameterized during feature detection to make the ORB algorithm scale invariant and uniformly distributed; then, the Hamming distance is used for feature matching, and the RANSAC algorithm [22] is used to remove the mismatching points; finally, the best stitching line is found by using a dynamic programming algorithm with low complexity, and the stitched image is found to be the best stitching line. Finally, the optimal suture line is found by using a dynamic planning algorithm with low complexity, and the stitched image is smoothed by Poisson fusion. The specific process is shown in Figure 3.

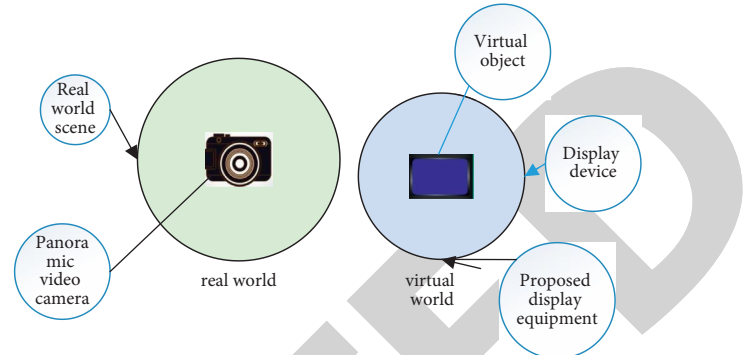


FIGURE 1: The principle diagram of the circular panoramic video AR system.

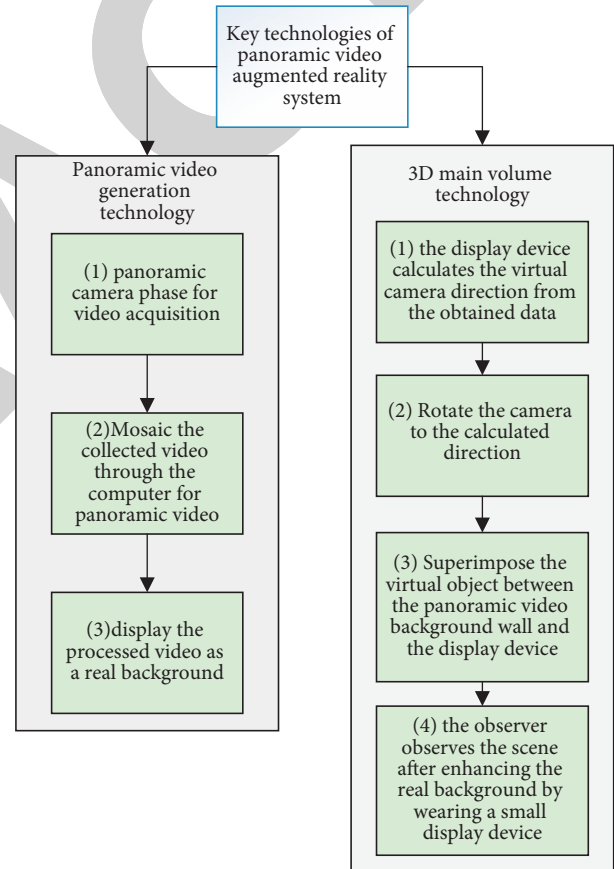


FIGURE 2: The key technologies of the panoramic video augmented reality system.

2. Improvement of the ORB Algorithm

2.1. Build the Scale Space and Find the Extreme Value Point. Under certain restricted conditions, the Gauss function is the only kernel smoothing function in the scale space [23]. The scale of the image $F(x, y)$ is defined as the function $L(x, y, \sigma)$, where σ is the scale factor, which is obtained by composing the image $F(x, y)$ with the Gauss function $G(x, y, \sigma)$ [24].

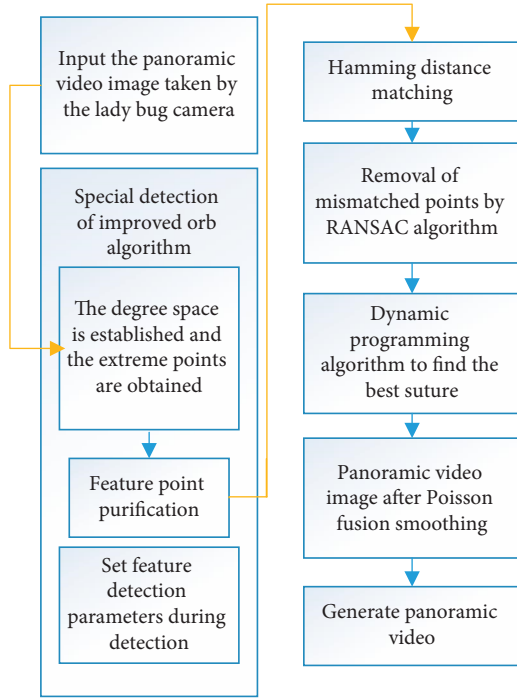


FIGURE 3: Flow of the improved ORB panorama video generation method.

$$L(x, y, \sigma) = G(x, y, \sigma)F(x, y),$$

$$G(x, y, \sigma) = \frac{1}{2\pi\sigma^2} \exp\left(-\frac{x^2 + y^2}{2\sigma^2}\right). \quad (1)$$

In order to obtain stable feature points in the scale space, the polar points are searched in the space $D(x, y, \sigma)$ obtained by image convolution with the Gauss difference function [25], and their local polar points are considered as the candidate feature points in the scale space with the relationship, as shown in the following equation:

$$D(x, y, \sigma) = [G(x, y, k\sigma) - G(x, y, \sigma)]F(x, y) \\ = L(x, y, k\sigma) - L(x, y, \sigma), \quad (2)$$

where the constant k separates the two adjacent scales.

2.2. Characteristic Point Purification. After the detection of the extreme points, some unstable extreme points are removed to make the feature matching more stable. The positions of the extreme points of the original image are calculated by using a 3-dimensional second-order function at a certain scale, and the low-contrast extreme points are removed. First, a Taylor expansion of $D(x, y, \sigma)$ is performed at an extreme point:

$$D(X) = D + \frac{\partial D^T}{\partial X} X + \frac{1}{2} X^T \frac{\partial^2 D}{\partial X^2} X. \quad (3)$$

By finding the partial derivative of \dot{X} from equation (3) and making it zero, we can obtain the extreme value point \dot{X} with the following equation:

$$\dot{X} = -\frac{\partial^2 D^{-1}}{\partial X^2} \frac{\partial D}{\partial X}. \quad (4)$$

Substituting equation (3) into equation (4), we have

$$D(\dot{X}) = D + \frac{1}{2} \frac{\partial D^T}{\partial X} \dot{X}. \quad (5)$$

If \dot{X} is present, the extreme points corresponding to it are removed, and the extreme points with low contrast are filtered out. The polar points on the edges are removed by calculating the ratio of the principal curvature to obtain stable polar points [26]. The Hessian matrix of the extreme points to be detected is calculated as follows:

$$H = \begin{pmatrix} D_{xx} & D_{xy} \\ D_{xy} & D_{yy} \end{pmatrix}. \quad (6)$$

Let the maximum and minimum eigenvalues of H be α and β , respectively:

$$\begin{cases} \text{Trace}(H) = D_{xx} + D_{yy} = \alpha + \beta, \\ \text{Det}(H) = D_{xx}D_{yy} - (D_{xy})^2 = \alpha\beta. \end{cases} \quad (7)$$

From equation (7), the principal curvature of the extreme point D is proportional to the eigenvalue corresponding to H . Let $\gamma = \alpha/\beta$; then, we have $(\text{Trace}(H)^2/\text{Det}(H)) = ((r+1)^2/r)$, and then as γ increases, $(r+1)^2/r$ also increases. Then, the ratio of principal curvature is checked by equation (9) to see if it is less than a certain threshold value γ :

$$\frac{\text{Trace}(H)^2}{\text{Det}(H)} = \frac{(r+1)^2}{r}. \quad (8)$$

Usually, the threshold $\gamma = 8$; i.e., the extreme points of a principal curvature ratio not greater than 8 are retained, and the other extreme points are removed.

2.3. Setting of Feature Detection Parameters. During feature detection, the number of extracted feature points is controlled by setting an integer N and setting the minimum spacing D between feature points so that the set of feature points is evenly distributed. If N is too small, it affects the uniform distribution of feature points. If N is too large for feature matching efficiency, N value can be obtained from the size of the reference image; if D is too large for feature matching success rate, D is too small for dense patches of feature distribution; D value can be set according to the demand of feature density [27]. In this paper, we set $N = 2,300$ and $D = 6$ px, where the values N and D are obtained experimentally.

Therefore, while retaining the advantages of fast operation and rotation invariance of the ORB algorithm, the ORB algorithm is made scale invariant, and the number of feature points and the spacing of feature points are parameterized in the feature extraction to make the feature distribution uniform [28].

2.4. Finding the Best Suture Line and Image Fusion. If the stitching is done directly after feature extraction and matching, it may make the panoramic video less effective due to the change of external ambient light. Unlike the traditional method of using motion estimation [29], the stitching crack “GHOST” phenomenon is suppressed by finding an optimal stitching line at the time of stitching and taking the content of one frame on both sides of this line to fill. A dynamic programming algorithm is a substratum of an optimal policy that must be optimal for its initial and final states. In applying the dynamic programming algorithm, suppose that there are n stages, $r_i(S_i, X_i)$ is the quantity indicator of the decision in stage i , S_i is the starting point of stage i , and X_i is the starting point of stage i and $i + 1$; then, the dynamic programming is to solve the value E :

$$E = \text{opt}[r_1(S_1, X_1) * \dots * r_n(S_n, X_n)], \quad (9)$$

where “*” is the operation symbol and opt is max or min. In solving the shortest path, opt is taken as min and “*” is taken as “+” in order to minimize the summation of the stages. Drawing on the idea of dynamic programming, the above equation is used as the criterion equation for solving the value of the strategy index. First, initialize; then, expand down the row of calculated suture strength until the last row; and finally, select the best suture with the smallest strength value from the resulting set of all sutures [17, 27].

At this point, the search for the best stitching line is completed, and then the Poisson fusion algorithm is used to smooth the stitched image so that the stitched video image can reach the requirement of seamless and eliminate the “GHOST” phenomenon.

3. Panoramic Video Image Alignment and Fusion

3.1. Projection Plane Alignment. The process of acquiring spatial extremes of the scale ensures that the panoramic video is output in real time with standard video positioning, and then an algorithm is used to obtain the relevant parameters for the optimal projection matrix to enable interframe alignment of the video. The implementation process is simplified by using an efficient method to project and fuse all video frames from different cameras [25]. The implementation process is based on the alignment parameters obtained from the primitive process, and the alignment is completed by projecting all frames from different cameras into the same plane, which is represented as follows:

$$\begin{cases} x' = \frac{u_0x + u_1y + u_2}{u_6x + u_7y + 1}, \\ y' = \frac{u_3x + u_4y + u_5}{u_6x + u_7y + 1}, \end{cases} \quad (10)$$

where the 8 parameters of the optimal projection matrix obtained during the priming process are described by $u_i (i = 0, 1, 2, \dots, 7)$, the left side of the pixel point in the

projection frame is described by (x, y) , and the coordinates of the pixel point projected into the reference frame are described by (x', y') .

In order to improve the image effect after alignment, we need to set up a large background image space and use this background image to align all frames. The reference coordinates used in the alignment process are the frame coordinates of the middle camera, and the background image is shaped according to these coordinates, i.e., the frames of the middle camera are filled into the middle of the background image, and the frames of other neighboring cameras are projected and transformed $W1$ and $W2$, respectively, and then aligned with the reference frames in the background image, and at the same time, the blending range between different frames is fused using bilinear fusion and nonlinear fusion techniques.

4. Hybrid Range Fusion

4.1. Bilinear Weighted Fusion. For example, if there are two frames in the blending range Q_1 and Q_2 and the weighting function is $a(x, y)$, the pixel value $E_{\text{hybrid}}(x, y)$ of the blending range of the fused frame can be expressed as

$$E_{\text{hybrid}}(x, y) = a(x, y) * Q_1(x, y) + (1 - a(x, y)) * Q_2(x, y). \quad (11)$$

Mixed range pixel values between adjacent frames are operated by bilinear weighted fusion [19]. The weighting function is shaped by the distance between the target pixel coordinates and the original frame boundary. Set the projected two images to be g and P , respectively, and a point in the mixing range of the two images to be s ; then, the pixel values of the point in the two images are S_G and S_P , respectively, the minimum distances of the operation point s from the four sides of the two images are J_G and J_P , and the pixel value S_{Blend} of the point s in the fusion image is obtained as follows:

$$S_{\text{Blend}} = \frac{J_G}{J_G + J_P} \cdot S_G + \left(1 - \frac{J_G}{J_G + J_P}\right) S_P. \quad (12)$$

Fused pixel values of equation (5) fully analyze the value of adjacent frames, and the fusion of a single pixel range to the mixed range can be accomplished under normal conditions, but when the image has a parallax problem, two frames of the mixed range need to be fused, and the difference in content is high, resulting in ghosting and blurring in the mixed range.

4.1.1. Nonlinear Fusion. If the observation point fluctuates, the relative distance between the same object and nearby objects fluctuates significantly, resulting in parallax. Especially, when the distance between the object and the camera is particularly small, it will form a serious parallax problem. In this case, a nonlinear template fusion method is used to

solve the ghosting problem by constructing a risk-weighted template function:

$$b(x, y) = \begin{cases} 1, & \min(x, y, |x - R|, |y - Z|) > M, \\ \frac{\{\sin(\pi \cdot (\min(x, y, |x - R|, |y - Z|)/M - 0.5)) + 1\}}{2}, & \text{otherwise,} \end{cases} \quad (13)$$

where R and Z denote the width and height of the original frame, respectively, and M denotes the width of the nonlinear transition range. The value of a in the center of the frame remains stable, and when it is close to a certain range of the boundary, it enters the transition range of width M , which decreases rapidly in a nonlinear manner, and the rate of decrease is regulated by the M value. The M value is used to adjust the respective weight and weighted areas of neighboring frames in the fusion process, and the higher the M value, the wider the transition range between neighboring frames and the smoother the transition, and vice versa. This nonlinear fusion process can adjust the transition rate and range at the boundary of the blending range in real time to solve the ghosting problem and enhance the fusion effect of the image [30–32].

5. Experimental Results and Analysis

5.1. Experimental Software and Hardware Platform. The video sequence-based environmental art design method was selected for comparison experiments. The experiment is divided into two parts: the simulation part compares the size of the shadow area visually through data software, and the actual test part compares the fusion effect to judge the advantages and disadvantages of the two methods. A special camera was used for data acquisition during the experiment, as shown in Figure 4, and relevant experimental parameters were given as shown in Table 1.

6. Simulation Experiment Results

The simulation results of the two environmental art design methods are shown in Figure 5. Among them, Figure 5(a) shows the deviation in positioning magnitude of the comparison method, and Figure 5(b) shows the deviation in positioning magnitude of this method. Since the experiments have eliminated all the influencing factors in the design process to the greatest extent, the analysis of Figure 5 shows that the common shadows in Figure 5(a) are larger and those in Figure 5(b) are smaller, which indicates that the comparison method fails to locate the object itself, resulting in the phenomenon of shadow superposition, while the design method in this paper is better.

6.1. Algorithm Performance. A panoramic video image of the Jinchengguan Intangible Cultural Heritage Exhibition Hall in Lanzhou city taken by a ladybug is simulated. The initial two frames shown in Figure 6 are compared with the ORB

algorithm for feature detection, and the results of the ORB algorithm are shown in Figure 7, and the results of the improved ORB algorithm are shown in Figure 8. The results of the ORB algorithm and the improved ORB algorithm are shown in Figure 7, respectively, after using Hamming distance to match the detected feature points and the RANSAC algorithm to remove the wrong matching points, and finally, the results of the improved ORB algorithm are shown in Figure 9, respectively, after using weighted average fusion and Poisson fusion smoothing.

In Figure 6, the gymnast identification and tracking system is mainly composed of two parts: hardware for image information data acquisition and software for machine vision identification and tracking.

The correlation R , entropy, spatial frequency, and average gradient indexes in [18] are used to quantitatively evaluate the fusion algorithm. R indicates the correlation between the stitched image and the original image, and ideally, R is 1; entropy is a measure of the average amount of information, and the larger the entropy value, the better the fusion effect; spatial frequency reflects the overall active level of the image, and the larger the value, the clearer the image; the larger the average gradient, the clearer the image. The results shown in Figure 10 are obtained statistically. It can be seen that the Poisson fusion algorithm has the highest R value and has advantages in entropy, spatial frequency, and average gradient.

The I-KCF and KCF target tracking algorithms are quantitatively analyzed in terms of success rate, which is evaluated in terms of the overlap rate of the border frames. Assuming that the tracked bounding boxes τ_t and τ_a are accurate bounding boxes, the repetition rate is defined as $s = (|\tau_t \cap \tau_a| / |\tau_t \cup \tau_a|)$, $|\cdot|$ denoting the number of pixels in the region; to evaluate the performance of the tracking algorithm in the video sequence, the number of successful frames with $S > t_0$ is calculated, and the results are shown in Figure 11.

The simulation results show that the panoramic video generation algorithm proposed in this paper has a good stitching effect and effectively suppresses the effects of stitching cracks and the “GHOST” phenomenon. The local enhancement effect of the I-KCF-based augmented reality 3D registration algorithm is good.

6.2. Superparameter Value of Our Network Loss Function. In order to test and verify the segmentation effect of the WBCE Tversky loss function used to train the main network



FIGURE 4: Experimental camera set.

TABLE 1: Experimental camera parameters.

Attribute	Value
Color (rgb)	24
Capture rate (cif)	30
Focal length	Manual balance
White balance	Brake balance
Exposure form	Braking exposure
Gain range (cm)	3
Signal-to-noise ratio	>48 dB
Camera lens	F1.8/F7.85
Focus range	>80 mm
Apparent elevation angle	50°
Current (mA)	200
Lighting (lux)	2.5

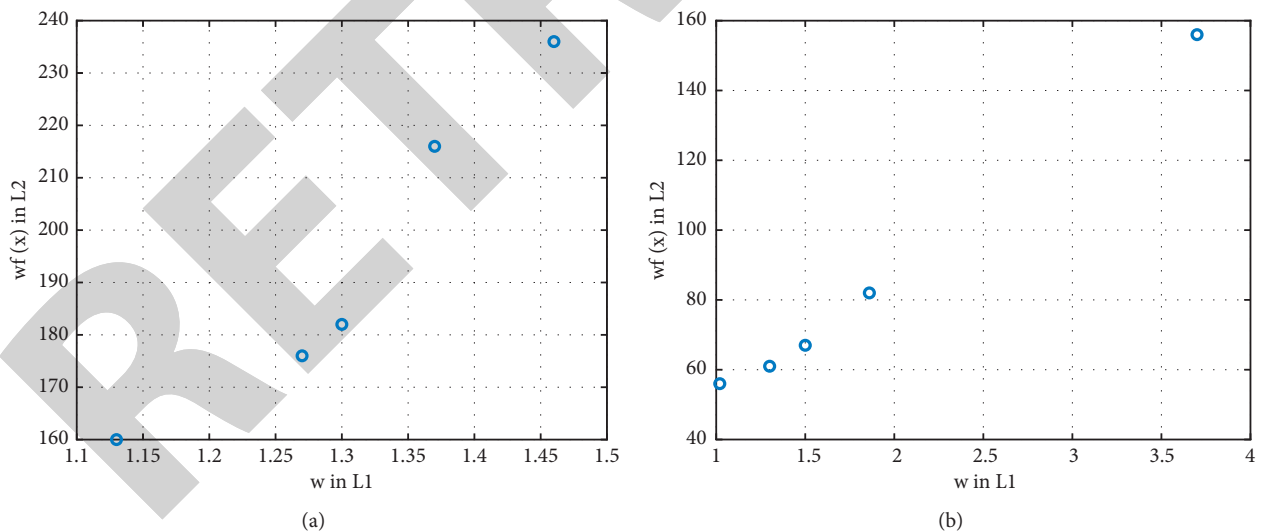


FIGURE 5: The average distribution of the weight.

of our network and to determine the superparameters β according to the range from 0.5 to 1.0, the value is compared in steps of 0.05 and compared with WBCE and Tversky loss function alone to prove the improvement of its performance. Based on GAN and Unet, the above different loss functions and parameter values are used for comparative experiments, and the experimental results are based on β . The values

obtained by different methods are drawn into a line graph as shown in Figure 12. The WBCE loss function has no superparameters β . The experimental results are as follows: DSC is 48.31%, F2 is 47.45%, PR is 65.17%, and re is 46.66%. Comparing the WBCE experimental results with Figures 12(a) and 12(b), it can be seen that β , the DSC, and F2 of the WBCE Tversky loss function are higher than



FIGURE 6: The initial image.



FIGURE 7: The ORB algorithm matching effect.

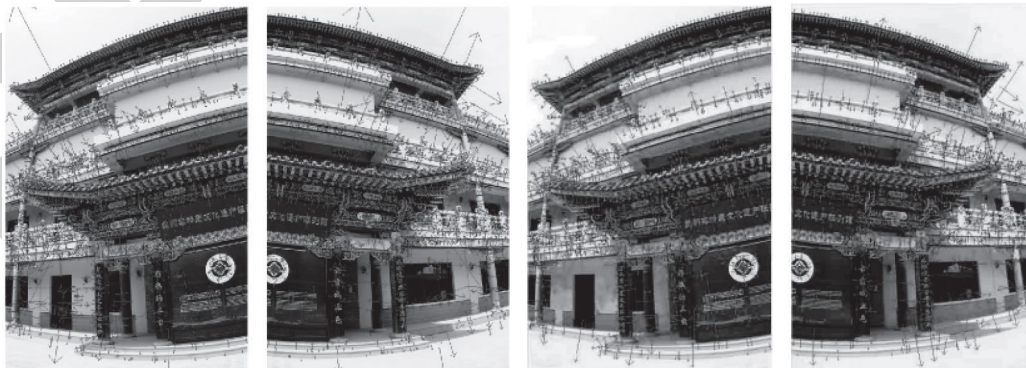


FIGURE 8: The ORB algorithm feature detection results.

Tversky and WBCE loss function. When $\beta = 0.8$, the WBCE Tversky loss function achieves the best segmentation performance. Science Tversky can adjust the accuracy and recall rate by adjusting the beta value. It can inhibit false negative and improve false positive, so as to improve the recall rate.

Therefore, with β , the accuracy decreases and the recall increases, which is consistent with the experimental results in Figures 12(c) and 12(d).

As mentioned earlier, the use of tolerance loss on the secondary network of our network can obtain moderate



FIGURE 9: The panoramic video image after stitching.

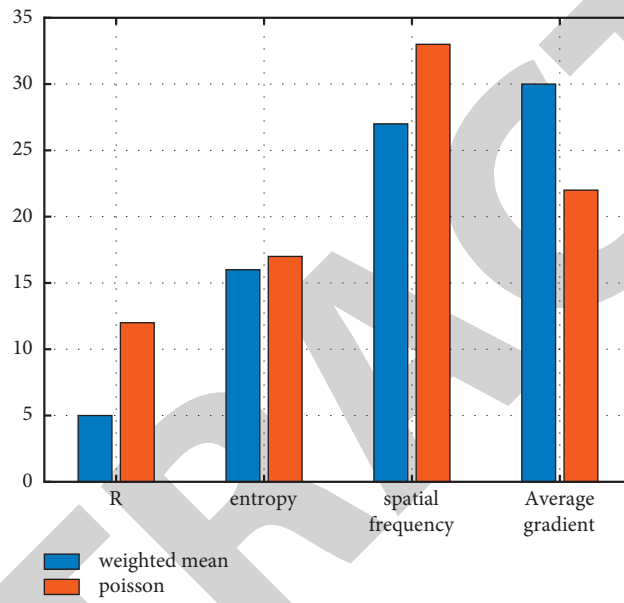


FIGURE 10: Convergence distribution of different methods.

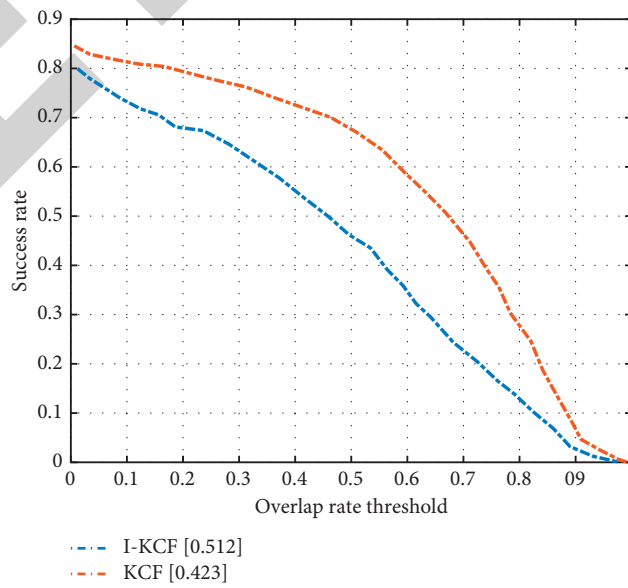


FIGURE 11: Success rate comparison chart.

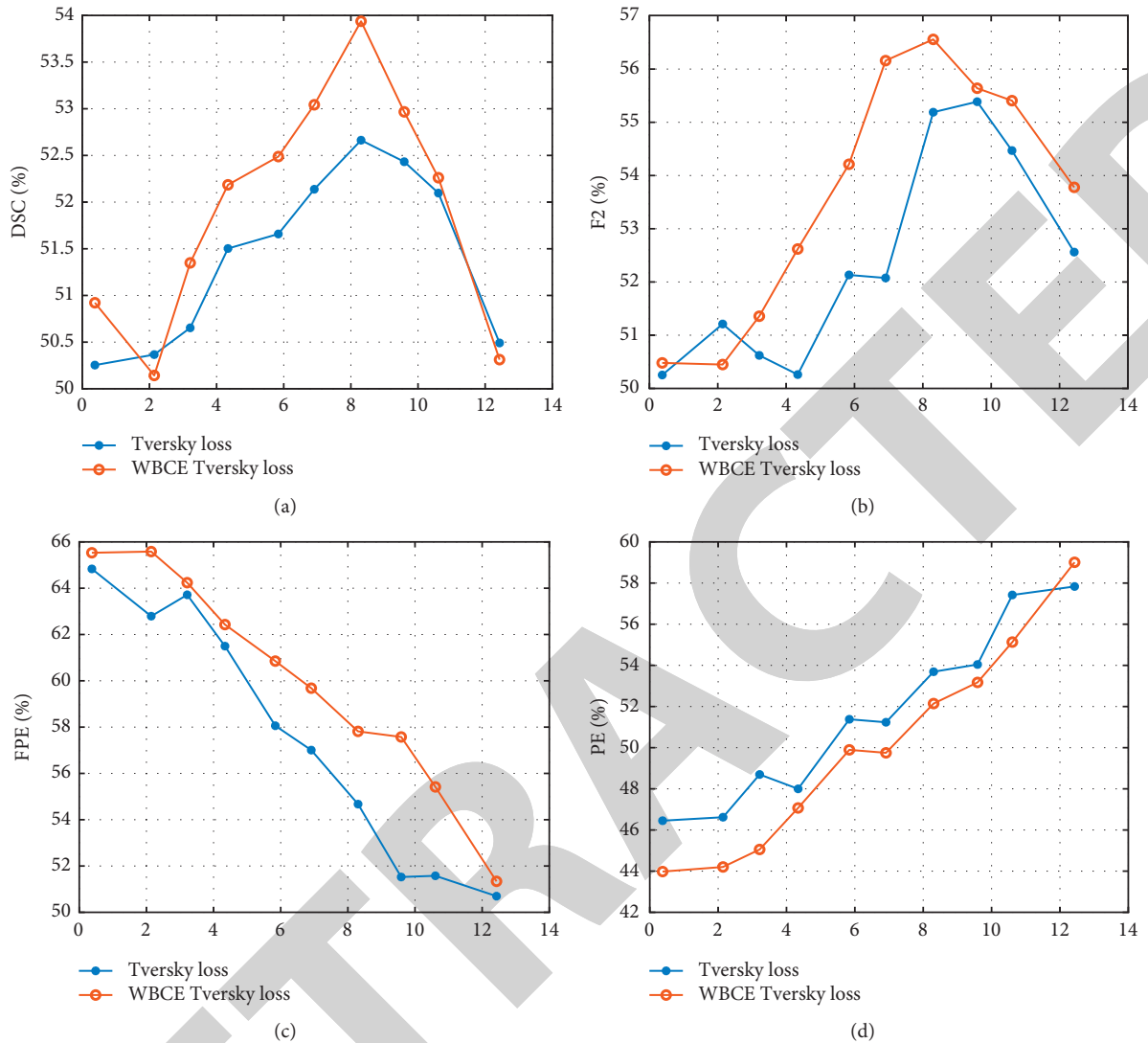


FIGURE 12: The performance comparison of WBCE Tversky and Tversky loss functions under different parameter configurations.

model constraints and a larger range of loss. Therefore, the parameters need to be adjusted, β , λ , and δ . Take appropriate values.

The training is still carried out on gau-a-unet, and the experimental results are drawn as a broken line diagram, as shown in Figure 13. In Figure 13(a), when the δ value remains unchanged, the higher the λ value, the higher the false-positive rate because the larger λ values provide greater weight for series items. And when the λ value remains the same, the smaller the δ value, the higher the false-positive rate because the specificity is δ value, which is considered as the training target. Hence, the smaller the δ value, the

smaller the specificity value. $F = 1 - s$, so the false-positive rate will increase with the decrease of specificity.

The false-positive rates corresponding to different values of λ and δ were sorted in the ascending order, as shown in Figure 13(b), and it can be seen that the false-positive rate gradually increased with the change of parameter configuration. When $\lambda = 5$ and $\delta = 0.6$, the false-positive rate achieves the maximum value, which is as high as 15.06%. From Figure 13(a), it can be seen that, for a pair of λ and δ values, the resulting false-positive rate is sometimes closer in value to that produced by using adjacent larger (or smaller) λ value and adjacent smaller (or larger) δ value, which means that

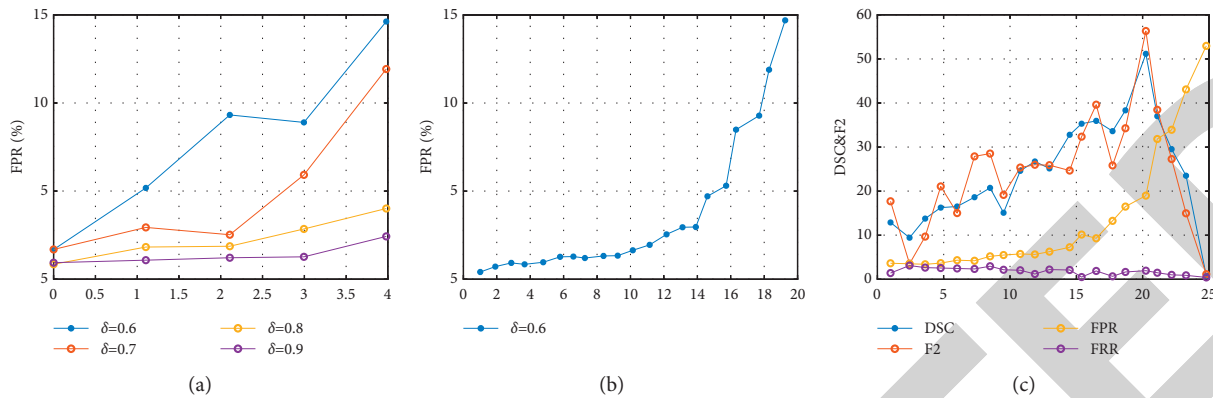


FIGURE 13: Different δ and λ values configure the false-positive rate curve under the tolerance loss function.

the magnitude of the false-positive rate is the result of the combined effect of λ and δ .

7. Conclusions

This paper proposes a new augmented reality system—the panoramic video augmented reality system. The two key technologies of panoramic video generation and augmented reality 3D registration to realize this system are studied, and the panoramic video stitching technology based on the improved ORB feature detection algorithm and the augmented reality 3D registration method based on I-KCF tracking are proposed. By adopting and improving the fast ORB feature detection algorithm and fast KCF target tracking algorithm, the panoramic video augmented reality system is more real time and noise-resistant, and the augmented reality technology is applied to the panoramic video imaging in this paper so that the scenes with added virtual information in the panoramic video can be viewed anytime and anywhere, which broadens the application fields of panoramic video and augmented reality and has certain practicality and innovation. The next step is to perform GPU acceleration on the graphics image processing algorithm.

Data Availability

The datasets used in this paper are available upon request to the author.

Conflicts of Interest

The author declares that there are no conflicts of interest regarding this work.

References

- [1] L. Kunming and D. Lina, "Research on the application of environmental art design based on digital media technology," *Journal of Physics: Conference Series*, vol. 1915, no. 2, Article ID 022072, 2021.
- [2] C. Xue, "Research on the expression of environmental art design based on virtual technology," *Revista de la Facultad de Ingenieria*, vol. 32, no. 9, pp. 560–565, 2017.
- [3] J. Zhao, "Research on the application of BIM in environmental art design," *IOP Conference Series: Earth and Environmental Science*, vol. 676, no. 1, Article ID 012018, 2021.
- [4] Z. Bo, X. Haitao, L. Lulu, J. Jun, Z. Jianyue, and T. Yiping, "Development of coordinate-machine of the scene of road traffic accident based on binocular stereo omni-directional vision sensors," *Procedia Engineering*, vol. 24, pp. 262–266, 2011.
- [5] J. Multisilta, "Editorial on mobile and panoramic video in education," *Education and Information Technologies*, vol. 19, no. 3, pp. 565–567, 2014.
- [6] "A Study on emotional touchpoint analysis by Eye-Tracking technology in dynamic environment - focused on automotive interior space," *Journal of Digital Design*, vol. 14, no. 2, pp. 285–294, 2014.
- [7] X. Yu and W. Wang, "Research ON the application OF waste residue IN environmental artisitic design[j]," *China Ceramics*, vol. 44, no. 11, pp. 85–87, 2008.
- [8] "Research on environmental art design system based on virtual reality technology," *Journal of Physics: Conference Series*, vol. 1992, no. 2, Article ID 022129, 2021.
- [9] R. Rosariastuti, S. Sudadi, and F. S. Prasasti, "A bioremediation process based on the application of *Rhizobium* sp. I3 and *Ramie* (*Boehmeria nivea* L.) in lead contaminated soils," *Journal fur Kulturpflanzen*, vol. 72, no. 2/3, pp. 40–48, 2020.
- [10] C. Zhang, T. Xie, K. Yang et al., "Positioning optimisation based on particle quality prediction in wireless sensor networks," *IET Networks*, vol. 8, no. 2, pp. 107–113, 2019.
- [11] S. Hao, "Research on the application of GIS technology in the preparation of village planning--Take Feng Sheng Village as an example," *IOP Conference Series: Earth and Environmental Science*, vol. 791, no. 1, Article ID 012150, 2021.
- [12] C. Krzysztof and J. Paweł, "The threat of environmental pollution with harmful substances, on the example of uncontrolled fires in landfills and actions aimed at reducing it," *Safety & Fire Technology*, vol. 57, no. 1, pp. 80–98, 2021.
- [13] J. W.-M. Yuen, I. Y.-P. Wong, P. K.-F. Chiu et al., "A comprehensive community-based prevalence study on nocturia in Hong Kong male adults," *International Journal of Environmental Research and Public Health*, vol. 18, no. 17, Article ID 9112, 2021.
- [14] C. Wang and R. Pawłowicz, "Internal wave generation from tidal flow exiting a constricted opening," *Journal of Geophysical Research: Oceans*, vol. 122, no. 1, pp. 110–125, 2017.

- [15] T. Xie, C. Zhang, Z. Zhang, and K. Yang, "Utilizing active sensor nodes in smart environments for optimal communication coverage," *IEEE Access*, vol. 7, pp. 11338–11348, 2018.
- [16] Z. Zhang, C. Zhang, M. Li, and T. Xie, "Target positioning based on particle centroid drift in large-scale WSNs," *IEEE Access*, vol. 8, pp. 127709–127719, 2020.
- [17] J. Fraser, R. Gupta, and M. E. Krasny, "Practitioners' perspectives on the purpose of environmental education: environmental education research," *Environmental Education Research*, vol. 21, no. 5, pp. 777–800, 2014.
- [18] H. El-Saied, A. H. Basta, and R. H. Gobran, "Research progress in friendly environmental technology for the production of cellulose products (bacterial cellulose and its application)," *Plastics Technology and Engineering*, vol. 43, no. 3, pp. 797–820, 2004.
- [19] D. S. Noonan, "Evidence of environmental justice: a critical perspective on the practice of ej research and lessons for policy design," *Social Science Quarterly*, vol. 89, no. 5, pp. 1153–1174, 2008.
- [20] L. Wang, C. Zhang, Q. Chen et al., "A communication strategy of proactive nodes based on loop theorem in wireless sensor networks," in *Proceedings of the 2018 Ninth International Conference on Intelligent Control and Information Processing (ICICIP)*, pp. 160–167, IEEE, Wanzhou, China, November 2018.
- [21] W. Li, "Application analysis of VR virtual technology in environmental art design teaching," *Journal of Physics: Conference Series*, vol. 1744, no. 4, Article ID 042222, 2021.
- [22] J. Qian, "Application of VR in art design," *Journal of Physics: Conference Series*, vol. 1533, no. 2, Article ID 022004, 2020.
- [23] H. Shi and D. Niu, "Application research of virtual reality technology in ocean environmental art design," *Journal of Coastal Research*, vol. 104, no. SI, pp. 296–301, 2020.
- [24] J. Long, Z. Yan, H. Chen, and X. Song, "Spectrum decomposition in Gaussian scale space for uneven illumination image binarization," *PLoS One*, vol. 16, no. 4, Article ID e0251014, 2021.
- [25] C. de Bérigny Wall and X. Wang, "InterANTARCTICA: tangible user interface for museum based interaction," *International Journal of Virtual Reality*, vol. 8, no. 3, pp. 19–24, 2009.
- [26] T. Portnova, "Information technologies in art monuments educational management and the new cultural environment for art historian," *TEM Journal*, vol. 8, no. 1, pp. 189–194, 2019.
- [27] I. Blečić, S. Cuccu, F. A. Fanni et al., "First-person cinematographic videogames: game model, authoring environment, and potential for creating affection for places," *Journal on Computing and Cultural Heritage (JOCCH)*, vol. 14, no. 2, pp. 1–29, 2021.
- [28] K. C. Su and K. C. Wu, "A crossover between 360 degree panoramic video, calligraphy art and fashion design," in *Proceedings of the 3rd Eurasian Conference on Educational Innovation 2020 (ECEI 2020)*, pp. 7–10, Hanoi, Vietnam, February 2020.
- [29] H. C. Pham, N. Dao, A. Pedro et al., "Virtual field trip for mobile construction safety education using 360-degree panoramic virtual reality," *International Journal of Engineering Education*, vol. 34, no. 4, pp. 1174–1191, 2018.
- [30] Y. Liu, S. Chen, and B. Guan, "Layout optimization of oil-gas gathering and transportation system in constrained three-dimensional space," *Chinese Science Bulletin*, vol. 65, no. 9, pp. 834–846, 2020.
- [31] Y. Liu, S. Chen, B. Guan, and P. Xu, "Layout optimization of large-scale oil-gas gathering system based on combined optimization strategy," *Neurocomputing*, vol. 332, no. 7, pp. 159–183, 2019.
- [32] B. Guan, S. Chen, Y. Liu, X. Wang, and J. Zhao, "Wave patterns of (2+1)-dimensional nonlinear Heisenberg ferromagnetic spin chains in the semiclassical limit," *Results in Physics*, vol. 16, Article ID 102834, 2019.